


On the Visibility of Prominence Fine Structures at Radio Millimeter Wavelengths

P. Heinzel¹ · A. Berlicki^{1,2} · M. Bárta¹ · M. Karlický¹ ·
P. Rudawy² 

Received: 25 February 2014 / Accepted: 2 June 2015 / Published online: 24 June 2015
© Springer Science+Business Media Dordrecht 2015

Abstract Prominence temperatures have so far mainly been determined by analyzing spectral line shapes, which is difficult when the spectral lines are optically thick. The radio spectra in the millimeter range offer a unique possibility to measure the kinetic temperature. However, studies in the past used data with insufficient spatial resolution to resolve the prominence fine structures. The aim of this article is to predict the visibility of prominence fine structures in the submillimeter/millimeter (SMM) domain, to estimate their brightness temperatures at various wavelengths, and to demonstrate the feasibility and usefulness of future high-resolution radio observations of solar prominences with ALMA (*Atacama Large Millimeter-submillimeter Array*). Our novel approach is the conversion of H α coronagraphic images into microwave spectral images. We show that the spatial variations of the prominence brightness both in the H α line and in the SMM domain predominantly depend on the line-of-sight emission measure of the cool plasma, which we derive from the integrated intensities of the observed H α line. This relation also offers a new possibility to determine the SMM optical thickness from simultaneous H α observations with high resolution. We also describe how we determine the prominence kinetic temperature from SMM spectral images. Finally, we apply the ALMA image-processing software Common Astronomy Software Applications (CASA) to our simulated images to assess what ALMA would detect at a resolution level that is similar to the coronagraphic H α images used in this study. Our results can

✉ P. Rudawy
rudawy@astro.uni.wroc.pl

P. Heinzel
pheinzel@asu.cas.cz

A. Berlicki
berlicki@astro.uni.wroc.pl

M. Bárta
barta@asu.cas.cz

M. Karlický
karlicky@asu.cas.cz

¹ Astronomical Institute, The Czech Academy of Sciences, 251 65 Ondřejov, Czech Republic

² Astronomical Institute, University of Wrocław, ul. Kopernika 11, 51-622 Wrocław, Poland

thus help in preparations of first ALMA prominence observations in the frame of science and technical verification tests.

Keywords Prominences, quiescent · Radio emission · Simulations

1. Introduction

Optical and UV spectral diagnostics has been extensively used to determine the basic plasma parameters of solar prominences, *i.e.* their kinetic temperature (Labrosse *et al.*, 2010). However, this approach has several drawbacks that are related to the complexity of the spectral line or continuum formation in this wavelength range. While optically thin lines sum up contributions from fine structures at different temperatures along the line of sight (LOS), optically thick lines require rather complex non-local thermodynamic equilibrium (NLTE) radiative-transfer treatment, and their shapes are strongly affected by the opacity effects. In view of these aspects, a temperature determination using optically thick lines is not straightforward. Moreover, several line-broadening mechanisms may distort the line shape, competing with the thermal broadening; for example, random motions of prominence fine structures along the LOS or the so-called microturbulence of unspecified origin (see *e.g.* recent analyses of the hydrogen H α line by Schmieder *et al.* (2010) and Gunár *et al.* (2012)). If we go beyond the temperature diagnostics and try to determine the temperature in the framework of energy balance models (Gouttebroze, 2007; Heinzel and Anzer, 2014), a full NLTE treatment of the radiative transfer for various lines and continua of many species is unavoidable.

The reported prominence temperatures range from low values between 4000 and 5000 K (see Hirayama (1990) and the Hvar Reference Atmosphere of Quiescent Prominences of Engvold *et al.* (1990)) up to almost coronal values. The latter are detected within the prominence-corona transition region (PCTR), using UV and EUV observations (Labrosse *et al.*, 2010). A common picture is that cool cores of prominence fine structures (threads) are surrounded by PCTR that are different along and across the magnetic field lines (Heinzel and Anzer, 2001; Gunár *et al.*, 2008). Lowest temperatures are consistent with some prominence models in radiation equilibrium (Heinzel and Anzer, 2014 and references therein), but higher temperatures of cool cores require some extra heating that is still a subject of debate. Realistic diagnostics of temperature and fine structures is therefore of crucial importance for our understanding of solar prominences.

The temperature determination is much more straightforward for radio observations at submillimeter/millimeter (SMM) wavelengths because it may serve as a direct ‘thermometer’ of the solar atmosphere (see *e.g.* Loukitcheva *et al.*, 2004; Heinzel and Avrett, 2012). In the case of prominences (both quiescent and eruptive), such SMM observations have been performed in the past mostly using a single-dish aperture that was able to provide only rather low (several or tens of arcsec) spatial resolution. Harrison *et al.* (1993) used the 15 m *James Clerk Maxwell Telescope* in Hawaii to perform first SMM observations of an active solar prominence at 1.3 mm, with a spatial resolution of about 20 arcsec. A more detailed study of filaments on the disk and a prominence on the limb was then performed by Bastian, Ewell, and Zirin (1993) at 0.85 and 1.25 mm, with a spatial resolution of 20 and 30 arcsec, respectively (using a single-dish 10.4 m telescope). These authors derived the maximum brightness temperature of the prominence to be 615 and 1480 K at 0.85 and 1.25 mm, respectively. From the ratio of observed brightness temperatures at these two wavelengths, they obtained the prominence optical thickness and kinetic temperature. They also derived the LOS emission measure of the cool prominence plasma of $1.3\text{--}2 \times 10^{29} \text{ cm}^{-5}$, which

implied an electron density of $1-3 \times 10^{10} \text{ cm}^{-3}$. Another example of SMM prominence observations is the study of Irimajiri *et al.* (1995), who used the Nobeyama 45 m radio telescope at 36 GHz, 89 GHz, and 110 GHz frequencies. These authors reported a kinetic temperature range between 5300 and 8000 K for a quiescent prominence, where the lower limit might be consistent with radiation equilibrium conditions. At centimeter wavelengths or longer, the prominence becomes optically very thick, and we see the hotter outermost layers of cool cores (see a review by Gopalswamy, Hanaoka, and Lemen, 1998). However, all previous SMM observations have been obtained with low spatial resolution, and thus they did not show the behavior of prominence fine structures.

Quite new perspectives appear with the construction of the *Atacama Large Millimeter/submillimeter Array* (ALMA) radio interferometer, operated by the European Southern Observatory, National Radio Astronomy Observatory, and National Astronomical Observatory of Japan. ALMA is located in Chile at the Atacama desert, on a plateau at 5000 m above the sea level. It will provide spectral observations in the wavelength range between 0.3 and 9 mm, with an unprecedented spatial resolution that reaches down to milliarcsec. While ALMA was primarily designed for stellar and extragalactic astronomy, it will be possible to perform solar observations in special modes as well (Karlický *et al.*, 2012). The aim of this article is to simulate what ALMA would detect of quiescent prominences and their internal structures. We show what a real prominence seen in the $H\alpha$ line would look like at different SMM wavelengths, taking into account the ALMA instrumental constraints. We also discuss the SMM-continuum formation under the typical prominence conditions and predict the range of brightness temperatures and continuum opacities for spatially resolved prominence structures. Finally, we discuss the problems of temperature diagnostics in the SMM domain.

This study is based on the $H\alpha$ coronagraphic observations of one particular prominence whose internal structure is clearly visible. The simulations we perform here provide synthetic radio millimeter images with a spatial resolution roughly an order of magnitude better than the above-mentioned SMM observations. This will be quite useful for first science and technical verification tests with ALMA.

2. Formation of SMM Radio Continua in Prominences

Under characteristic prominence conditions, the dominant source of opacity is the hydrogen free-free continuum for which the absorption coefficient at frequency ν is given as (Rybicki and Lightman, 1979),

$$\kappa_{\nu}(\text{H}) = 3.7 \times 10^8 T^{-1/2} n_e n_p \nu^{-3} g_{\text{ff}}, \quad (1)$$

where n_e and n_p are the electron and proton densities, T is the kinetic temperature, and $g_{\text{ff}} \approx 1$ is the Gaunt factor (cgs units are used). At low temperatures, H^- free-free opacity can also play a role. According to Kurucz (1970), we can write

$$\kappa_{\nu}(\text{H}^-) = \frac{n_e n_{\text{HI}}}{\nu} x, \quad (2)$$

where n_{HI} is the neutral hydrogen density, and x has the form

$$x = 1.3727 \times 10^{-25} + (4.3748 \times 10^{-10} - 2.5993 \times 10^{-7}/T)/\nu. \quad (3)$$

Finally, the total free–free absorption coefficient, corrected for stimulated emission, is

$$\kappa_\nu = [\kappa_\nu(\text{H}) + \kappa_\nu(\text{H}^-)](1 - e^{-h\nu/kT}), \tag{4}$$

where h and k are the Planck and Boltzmann constants, respectively (Rybicki and Lightman, 1979). Note that the stimulated emission term is non-negligible in the radio domain.

Two remarks are important here. First, at low temperatures, for instance, below 5000 K, hydrogen is much less ionized, and the ionization degree defined as $i = n_p/n_{\text{H}}$ goes to zero (n_{H} is the total hydrogen density). We can express the ratio $r = \kappa_\nu(\text{H}^-)/\kappa_\nu(\text{H})$ as

$$r = 2.7 \times 10^{-9} \nu^2 T^{1/2} x(1 - i)/i. \tag{5}$$

Gouttebroze, Heinzel, and Vial (1993) computed a set of low-temperature isothermal-isobaric models with $T = 4300$ K, which is the radiative-equilibrium temperature obtained by Heasley and Mihalas (1976). At this extremely low temperature, i decreases with increasing gas pressure; for the highest considered pressure $p = 1$ dyn, one obtains cm^{-2} , $i = 2.3 \times 10^{-2}$. But even under such extreme conditions, r is on the order of 10^{-4} in the wavelength range between 1 and 9 mm, and therefore we can neglect the H^- free–free opacity in prominences, contrary to the situation around the solar temperature minimum.

The second remark concerns the form of $\kappa_\nu(\text{H})$. In the literature, many authors used the form

$$\kappa_\nu(\text{H}) = \alpha n_e n_p T^{-3/2} \nu^{-2} \tag{6}$$

(Irimajiri *et al.*, 1995; Gopalswamy, Hanaoka, and Lemen, 1998; Loukitcheva *et al.*, 2004), where $\alpha = 0.018 g_{\text{ff}}$. In the radio domain, $h\nu/kT \ll 1$ and the stimulated emission term used in Equation (4) can be written simply as $h\nu/kT$. Using this term, we obtain Equation (6), which already includes the stimulated emission.

The synthetic intensity I_ν , emergent from the prominence on the limb, is in general obtained as

$$I_\nu = \int B_\nu(T) e^{-t_\nu} dt_\nu = \int \eta_\nu e^{-t_\nu} dl, \quad \eta_\nu = \kappa_\nu B_\nu, \quad dt_\nu = \kappa_\nu dl, \tag{7}$$

where $B_\nu(T)$ is the Planck source function, η_ν the emission coefficient, t_ν the optical depth, and l is the geometrical path length along the LOS. For simplicity we have omitted the μ -dependence of the specific intensity (μ is the cosine of the viewing angle). Free–free processes are collisional processes, and thus the corresponding source function is the Planck function (Mihalas, 1978). However, this does not mean that the continuum is formed by the LTE processes (*i.e.* the Saha equation for ionization). Under typical prominence conditions, n_e and n_p are governed by NLTE radiative transfer through hydrogen and helium continua where the photoionization and spontaneous recombination processes play a dominant role for the ionization equilibrium (Heinzel, 2014).

In the radio domain, I_ν and B_ν are directly proportional to the brightness temperature T_b and to the local plasma (kinetic) temperature T , respectively (*e.g.* Rybicki and Lightman, 1979)

$$I_\nu = \frac{2\nu^2 k}{c^2} T_b, \quad B_\nu = \frac{2\nu^2 k}{c^2} T, \tag{8}$$

where c is the speed of light. Using this Rayleigh–Jeans law, Equation (7) can be written as

$$T_b = \int T e^{-t_\nu} dt_\nu = \int T e^{-t_\nu} \kappa_\nu dl. \tag{9}$$

In the simplest case, assuming a uniform kinetic temperature T along the LOS, we obtain for a prominence slab of total optical thickness τ_ν

$$T_b = T(1 - e^{-\tau_\nu}), \quad (10)$$

where $\tau_\nu = \kappa_\nu L$ and L is the *effective* geometrical thickness of the prominence along the LOS representing the absorbing path. In all the following sections we only consider the free-free absorption according to Equation (6). In the optically thin limit we simply obtain $T_b = T\tau(\nu)$, which can be expressed as

$$T_b = \alpha \nu^{-2} T^{-1/2} \text{EM}, \quad (11)$$

where $\text{EM} = n_e^2 L$ is the emission measure. As we see from these relations, the brightness temperature of the prominence at a given position and a given wavelength thus depends on the kinetic temperature and optical thickness. The latter is directly proportional to the emission measure, provided that $n_e = n_p$ (this applies to a pure hydrogen plasma).

To account for low spatial resolution in the plane of sky, the surface filling factor is usually introduced; this represents the fraction occupied by prominence fine structures. The right-hand side of Equation (10) has to be multiplied by this factor (*e.g.* Irirajiri *et al.*, 1995). Therefore, at low spatial resolution we always obtain a lower-limit estimate for T if this filling factor is neglected (*i.e.* set to unity).

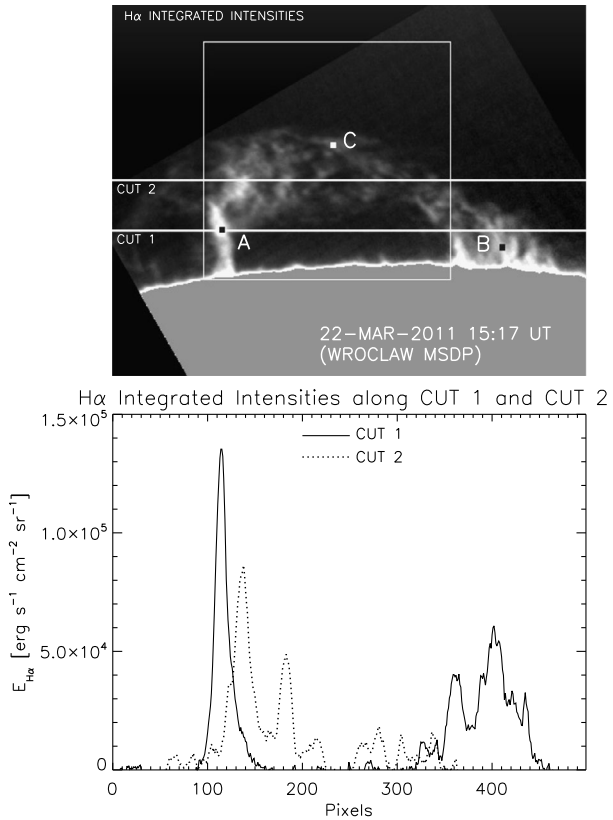
3. Simulations of the Brightness Temperature

To simulate the ALMA visibility of a quiescent prominence, and particularly its fine structures, we have used the following approach. We started from the $\text{H}\alpha$ prominence observations, and from a two-dimensional (2-D) quantitative spectroscopy we derived EM of the cool plasma at each pixel. Then we assumed a uniform kinetic temperature for all pixels and computed the spatial distribution of the brightness temperature. As a reference kinetic temperature we chose $T = 8000$ K. In reality, the spatial variations in T will also affect the distribution of T_b , but much less than the spatial variations of EM, which are substantial and are directly related to the $\text{H}\alpha$ image intensity (see discussion in Section 4.2). In these simulations we only considered cool cores of prominence structures and neglected any effects of a PCTR, similarly to the analysis of a quiescent prominence made by Bastian, Ewell, and Zirin (1993). This seems to be a good approximation for estimating a *lower limit* to the prominence SMM brightness. In reality, the prominence structures will be brighter and spatially more extended, which is consistent with some existing observations obtained with low resolution.

3.1. $\text{H}\alpha$ Prominence Observations

$\text{H}\alpha$ observations of a quiescent prominence were obtained on 22 March 2011 with the *Multichannel Subtractive Double Pass* (MSDP) spectrograph attached to the Large Coronagraph of the Astronomical Observatory of the University of Wrocław (Mein, 1991; Rompolt *et al.*, 1994). During the day, between 14:32 and 15:39 UT we completed about 70 scans over the prominence. Each scan consisted of 20 spectral images recorded with Photometrics KAF1400 12-bit CCD camera and covered effectively an area of about 380×170 arcsec in the plane of sky. The exposure time of the individual image was only 40 ms, while the

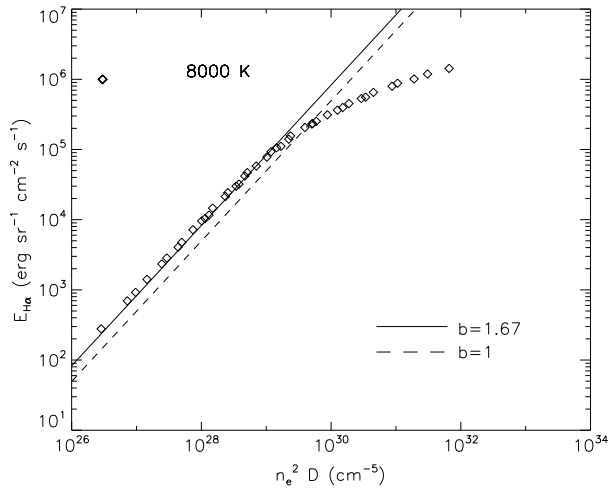
Figure 1 Top: H α prominence image as constructed from MSDP line-integrated intensities. The prominence was observed on 22 March 2011 at 15:17 UT. The field of view is 350 arcsec \times 270 arcsec (500 \times 390 pixels). CUT 1 and CUT 2 denote the lines used to show the spatial variations of integrated intensity, brightness temperature, and optical thickness quantitatively. Areas A, B, and C are the places at which the SMM spectrum was calculated. Finally, the white square box denotes a selected part of the prominence, whose simulated ALMA observations at 100 GHz are presented in more detail. Bottom: Variations of the H α integrated intensity along two cuts (CUT 1 and CUT 2) through the prominence.



time interval between two consecutive exposures was equal to nearly 2 s. Recording of the whole scan lasted about 47 s. For each scan we constructed a set of thirteen narrow-band images of the whole region (up to ± 1.2 Å from the H α line center), as well as the H α line profile at each pixel in the field of view. The spatial resolution of the obtained images was limited by seeing, on average to about 1 arcsec.

For our analysis, we used the MSDP spectral image obtained at 15:17 UT. We selected one of the highest resolution images, in which the prominence fine structure is well visible. This quiescent-type prominence was located on the northeastern limb of the solar disk (PA = 30°, Figure 1). After standard MSDP data processing (Mein, 1991), the observations were calibrated photometrically using a mean H α line profile averaged over a quiet region on the disk in the vicinity of the prominence. The photometric calibration was made by fitting the mean observed quiet-Sun profile to the reference quiet-Sun line profiles published by David (1961) and using the standard values of the limb-darkened continuum intensity near the H α line. We also corrected the data for scattered light by analyzing the MSDP signal in the ambient corona. After these photometric corrections we obtained absolutely calibrated H α line profiles of the prominence at each pixel of the MSDP image. From these we calculated the integrated intensities of the H α line, $E(\text{H}\alpha)$. The integration interval was ± 1 Å. Figure 1 presents a map of the H α integrated intensities computed for the MSDP image of the prominence obtained at 15:17 UT. It also shows the intensity variations along two selected cuts through the prominence. The behavior at three points A, B, and C with different brightness is discussed below.

Figure 2 Theoretical integrated emission of the H α line as a function of the emission measure, for isothermal prominence slabs with $T = 8000$ K (diamonds), according to Gouttebroze, Heinzel, and Vial (1993). Two lines represent an analytical fit given by Equation (12), with two different departure factors b ; see the text for details. Adapted from Jejčić and Heinzel (2009).



3.2. Emission Measure

After determining $E(\text{H}\alpha)$ at each pixel in the prominence, we converted this quantity to EM by using the well-established correlation described by Gouttebroze, Heinzel, and Vial (1993), Heinzel, Gouttebroze, and Vial (1994), and Jejčić and Heinzel (2009). This theoretical correlation is based on a set of isobaric-isothermal NLTE prominence models. The important result is that it is only very weakly dependent on the prominence kinetic temperature, and thus $E(\text{H}\alpha)$ provides a reliable diagnostics of the LOS emission measure of the cool plasma. We show this correlation in Figure 2, plotted for a temperature $T = 8000$ K. When $E(\text{H}\alpha)$ reaches a value of about 10^5 , the intensity starts to saturate because the H α line becomes optically thick. This result was obtained from 1-D slab models of arbitrary optical thickness. However, the prominences on the limb, particularly their fine structures, are mostly thin in the H α line, and thus the optically thin regime, where the plot shows a linear correlation, is a good approximation independent of the geometry and is applied in this study. For this, Jejčić and Heinzel (2009) derived the analytical formula

$$E(\text{H}\alpha) = 3.96 \times 10^{-20} b T^{-3/2} \exp^{17534/T} \text{EM}, \tag{12}$$

where b is the NLTE departure factor for the third hydrogen atomic level. For $T = 8000$ K, this factor is slightly larger than one (see the corresponding full line in Figure 2), while under the LTE conditions $b = 1$. For other temperatures, b is tabulated in Jejčić and Heinzel (2009). For brighter prominences, one should use the correlation curve as displayed in Figure 2. The derived value of EM is then used to compute the optical thickness at SMM wavelengths.

4. SMM Visibility of Prominence Fine Structures

The question frequently asked is to what extent the prominence fine structures, typically visible in optical lines such as H α or Ca II H or K (see *e.g.* excellent movies¹ from *Hinode/SOT* (Tsuneta *et al.*, 2008)), would be detectable with ALMA at SMM. To demonstrate this, we

¹http://hinode.nao.ac.jp/news/OldNews2007/071207PressRelease/okamoto1_yellow.mpg.

used the emission measure determined in the previous section to simulate the prominence images at various wavelengths covered by ALMA. For this we assumed a uniform temperature of 8000 K, which is a typical value for quiescent prominences. In reality, the temperature of the cool plasmas may vary between about 6000 K and 10 000 K (neglecting PCTR), for example, but this is of a secondary importance for our image simulations as we show below. The primary quantity is the emission measure EM, which we calculated at each pixel in our H α image. EM and T were then used to compute the SMM optical thickness at each pixel and the resulting brightness temperature T_b according to Equation (10). Since τ_ν is proportional to EM and the H α line integrated intensity is also proportional to it, we can derive a simple dependence of the SMM optical thickness on $E(\text{H}\alpha)$ using Equations (6) and (12). We obtain the relation

$$\tau(\nu) = 4.55 \times 10^{17} g_{\text{ff}} f(T) E(\text{H}\alpha) / \nu^2, \quad (13)$$

where

$$f(T) = \exp(-17534/T) / b(T) \quad (14)$$

is very weakly dependent on T . Using factors $b(T)$ from Jejčič and Heinzel (2009), we obtained $f(T) = 7.17 \times 10^{-2}$, 6.69×10^{-2} , and 5.83×10^{-2} for $T = 6000$ K, 8000 K, and 10 000 K, respectively. While we considered unsaturated H α intensities with $E(\text{H}\alpha) \leq 10^5$, $\tau(\nu)$ at SMM may still reach values well above unity. This SMM optical thickness then appears in Equation (10).

The resulting brightness temperatures T_b are shown in Figures 3 and 4 for three different wavelengths covered by ALMA (ALMA covers the spectral range roughly from 0.3 to 9 mm). From Equation (6) or (13) we immediately see that the opacity and thus τ_ν decreases with an increasing frequency. This has a direct consequence on the brightness temperature: for the optically thick structures, T_b saturates to a kinetic temperature T , while for thin cases we have $T_b < T$. This general behavior is clearly visible in our maps of T_b . We see that at $\lambda = 0.45$ mm the brightness temperature is very low, reaching at most 100 K, while at $\lambda = 9$ mm it almost saturates to a kinetic temperature of 8000 K in the brightest (*i.e.* most opaque) structure; see also CUT 1 and CUT 2 in Figure 5.

In reality, shorter wavelengths will show a sort of ‘mean’ T_b along the LOS, while at $\lambda = 9$ mm the surface fine structures should dominate because of the large optical thickness in the brightest structures. It is also clear that our method of converting the H α image into the ALMA image preserves the original spatial resolution of the MSDP image used. From these results we can immediately conclude that such a typical quiescent prominence will be clearly detectable with ALMA, especially at T_b below 10^3 K where the solar observations by ALMA are expected to be most efficient. This is further discussed together with the question of spatial resolution of ALMA in Section 5.

4.1. Optical Thickness

In Figure 5 we show the spatial variations of the optical thickness for three wavelengths, along CUT 1 and CUT 2 shown in Figure 1. At $\lambda = 0.45$ mm the structures are substantially optically thin, and thus T_b is far below T . At $\lambda = 3$ mm, the prominence is still optically thin, but T_b around 2000 K should be quite well detectable with ALMA. Bastian, Ewell, and Zirin (1993) claimed that prominences start to be optically thick at around 2.5 mm, but this is certainly case dependent; our prominence is rather faint, which is also reflected in low H α intensities. For this reason, we have assumed an optically thin case for the H α line,

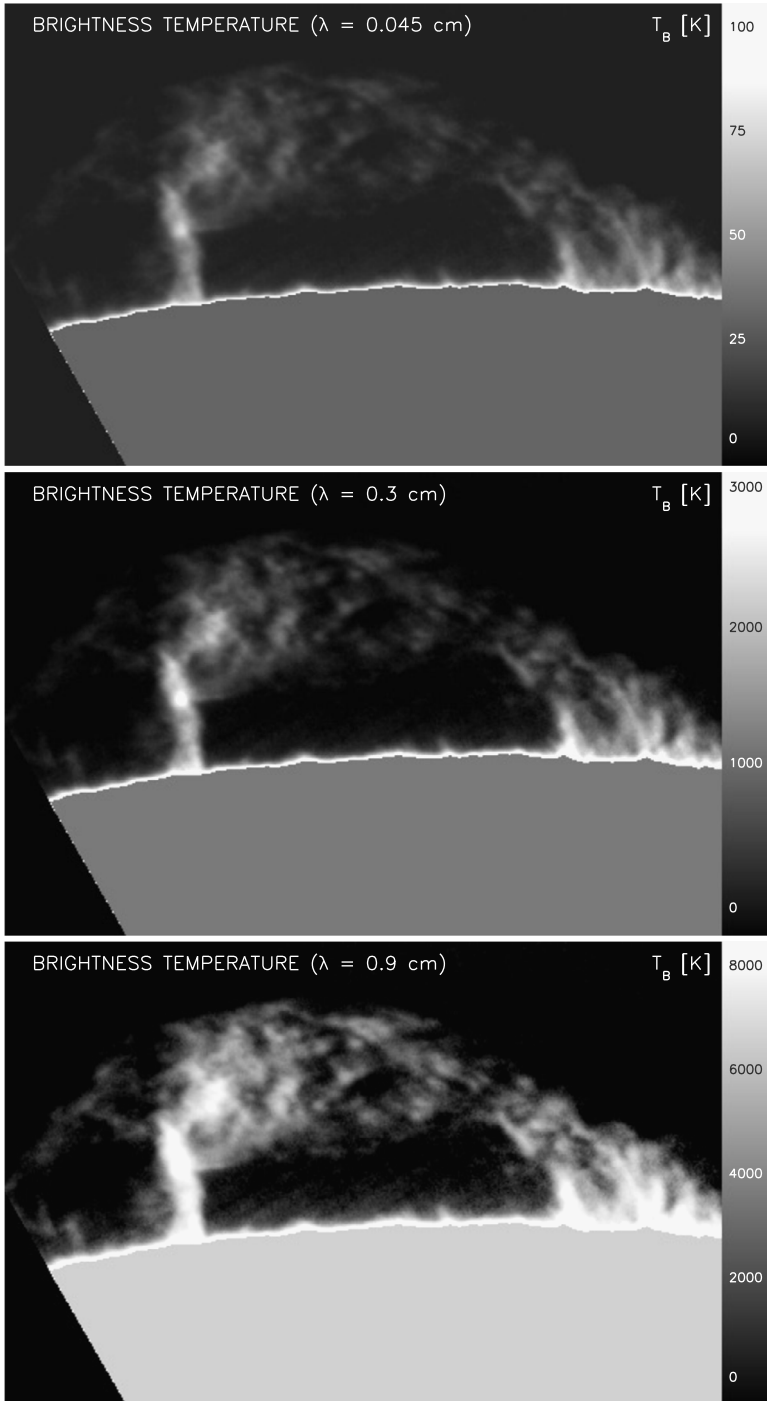


Figure 3 Simulated brightness temperature maps at 0.45 (top), 3 (middle), and 9 (bottom) mm. The field of view is $330 \text{ arcsec} \times 210 \text{ arcsec}$ (470×300 pixels). The spatial resolution here is the same as the original one for the $H\alpha$ coronagraphic image.

Figure 4 Simulated brightness temperature at 0.45 (top), 3 (middle), and 9 (bottom) mm plotted along the two cuts through the prominence shown in Figure 1. The pixel size is 0.7 arcsec.

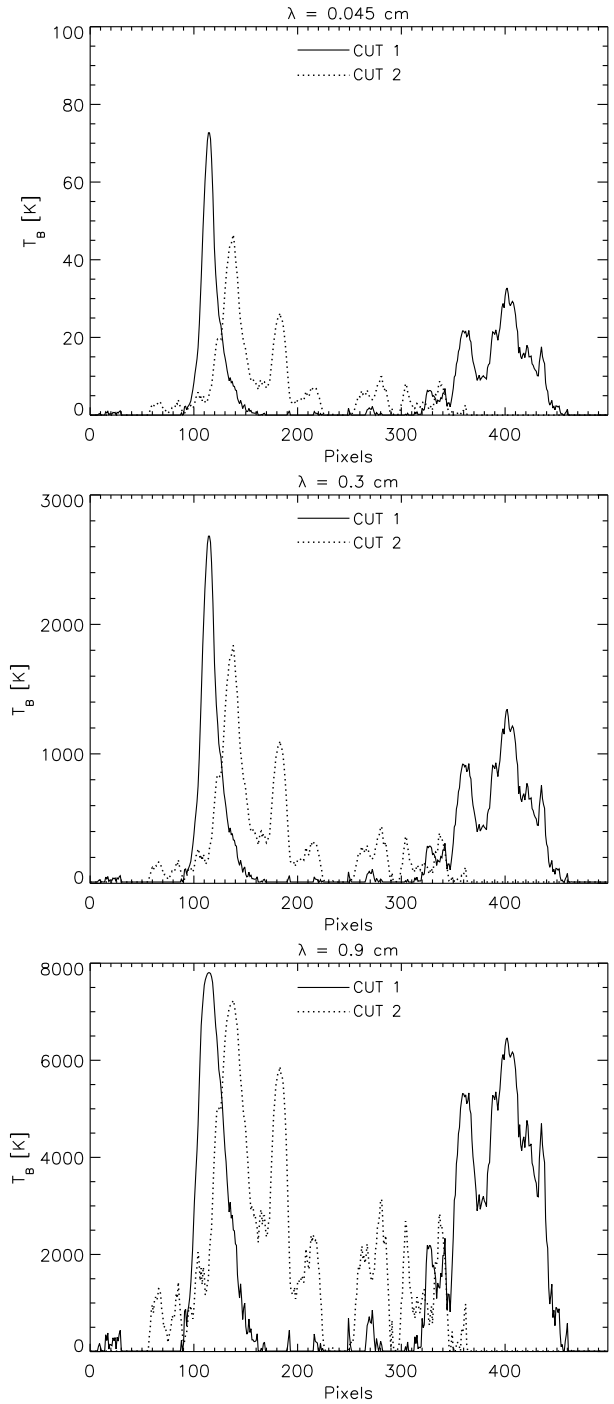
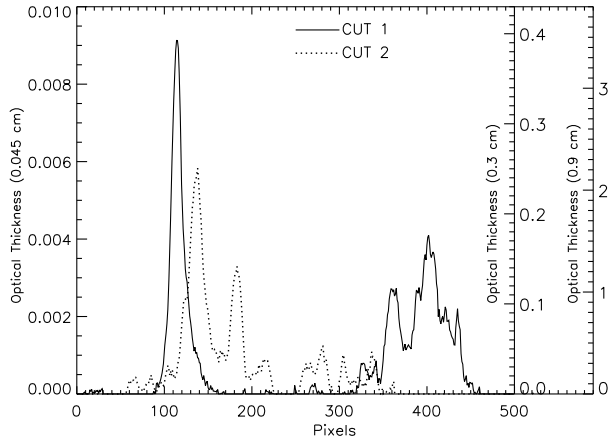


Figure 5 Simulated SMM optical thickness at 0.45, 3, and 9 mm plotted along the two cuts through the prominence shown in Figure 1. The pixel size is 0.7 arcsec.

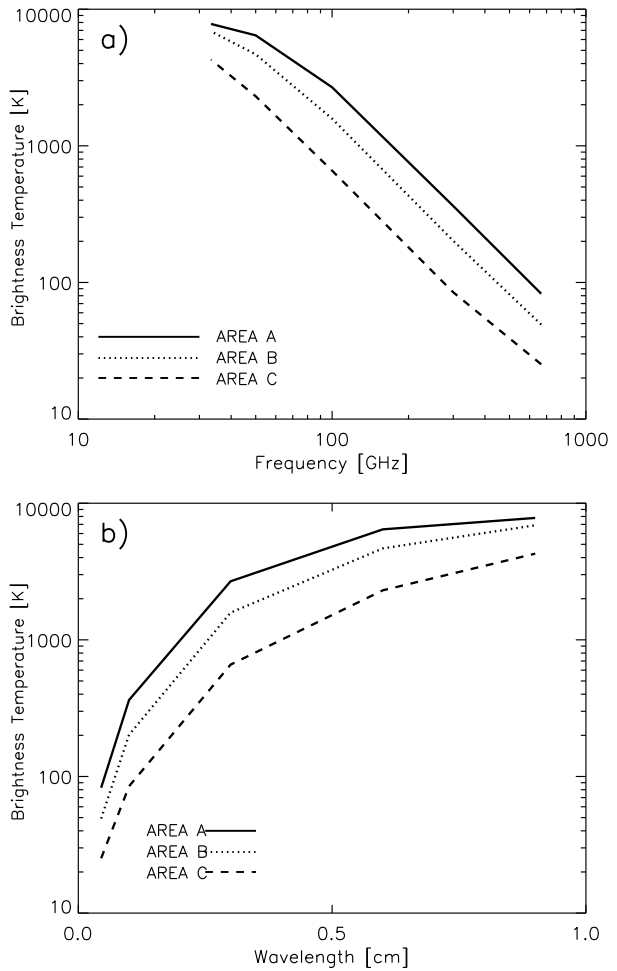


but there is no such assumption concerning the SMM wavelengths. In fact, at $\lambda = 9$ mm the prominence is already optically thick at the brightest areas where T_b saturates to T . We note that Irimajiri *et al.* (1995) obtained $\tau = 5.8$ at 8.3 mm. All optical thickness computations in our study here are based on the simplification that the free-free Gaunt factor is of the order of unity. In fact, g_{ff} in the ALMA SMM range and for low kinetic temperatures below 10^4 K is somewhat larger, reaching the values 3–4 (Karzas and Latter, 1961; Rybicki and Lightman, 1979). This will proportionally increase the optical thickness and thus T_b , but our results will remain qualitatively similar. It is somewhat appealing that some authors set the α -parameter in Equation (6) to (2), which implies very high Gaunt factors, reaching values of 10 (Dulk, 1985; Benz, 1993; Gopalswamy, Hanaoka, and Lemen, 1998).

4.2. Spectral Variations of Brightness Temperature

We have selected three representative brightness structures within the prominence (see areas A, B, and C marked in Figure 1) and computed the radio SMM spectrum. $T = 8000$ K and EM are those used previously. In Figures 6(a) and 6(b) we show the synthetic spectra using both the frequency and wavelength scales, respectively. We note that the spectral shapes computed under the assumption that the prominence is optically thin in SMM along the LOS would result from Equation (11), where we see that the brightness temperature mostly depends on EM, while its dependence in T is much weaker. This then means that real spatial variations in T_b will not differ much from those presented in Figure 3, provided that T is in the range of 6000–10 000 K. We again see that T_b at the longest wavelengths of ALMA almost saturates to $T = 8000$ K for the brightest area A. This is because $\tau > 1$ at those wavelengths. Simultaneously, the optically thin approximation is no longer accurate for these wavelengths. We note that the same behavior was demonstrated observationally for a quiescent prominence by Irimajiri *et al.* (1995), who used low-resolution observations taken with the 45 m radio telescope of the Nobeyama Radio Observatory, NAOJ. For a quiescent prominence they obtained $T_b = 5300$ K, 3300 K, and 2600 K at 36 (8.3), 89 (3.4), and 110 (2.7) GHz (mm), respectively; see also the spectral plot in their Figure 3. The kinetic temperature and the optical thickness are derived by fitting the SMM spectra. Here it is important to note that observing only at wavelengths where the prominence is optically thin does not allow distinguishing between T and τ because the ratio of the two values of T_b is just proportional to the ratio of λ^2 . However, having also the spectra at optically thick

Figure 6 Computed SMM radio spectra for the prominence on 22 March 2011, in terms of frequency (a) and wavelength (b). The spatial filling factor was not applied in these simulations.



wavelengths, both T and τ can be obtained by fitting the whole spectrum. Bastian, Ewell, and Zirin (1993) used Equation (10) at two wavelengths and derived the optical thickness and then the kinetic temperature from the observed ratio of the brightness temperatures.

5. Simulated ALMA Prominence Imaging

To demonstrate the feasibility of observations of solar prominences and their fine structures with ALMA, we have performed simulated observation (imaging) and its subsequent analysis using the tasks `simobserve()` and `simanalyze()` from the standard Common Astronomy Software Applications (CASA; see <http://casa.nrao.edu/>) package.

From the three model brightness maps at 0.45 mm, 3 mm, and 9 mm (see Figure 3), we chose the one at 3 mm (corresponding to 100 GHz) for further analysis. The map at 9 mm is at too low a frequency outside of the currently available ALMA frequency range. On the other hand, `simobserve()` requires – quite naturally – the pixel size in the input model image to be smaller than the ALMA resolution in a given configuration. Since our model data

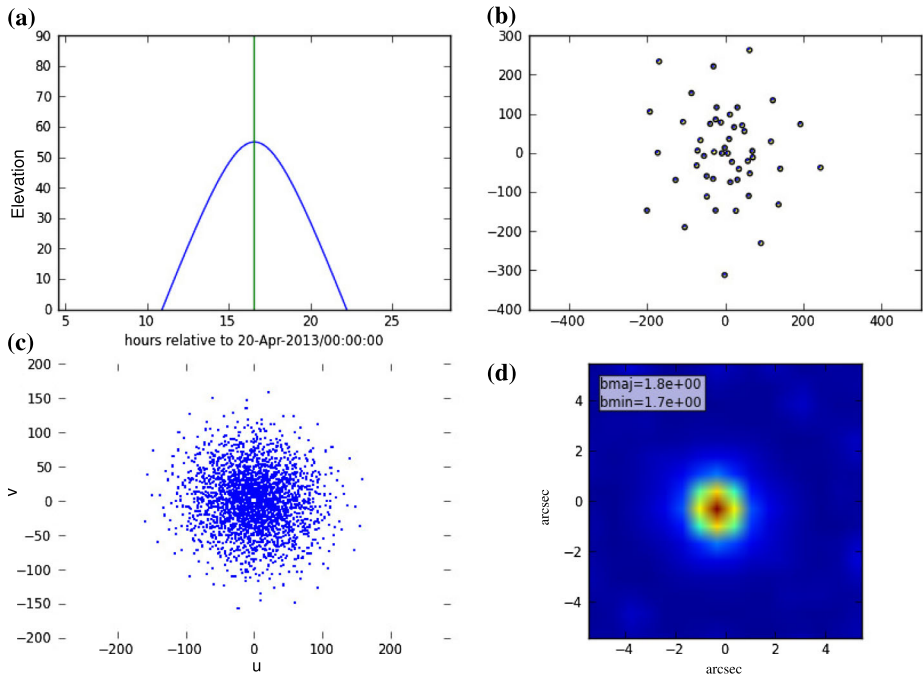


Figure 7 Simulated observation setup. (a) Elevation of the source. The simulated observation has been performed at its smallest zenith distance, *i.e.* local noon (denoted by the green line). (b) Positions of 12 m ALMA antennas (in meters) for the configuration ALMA-07 used for the simulation. (c) The $u-v$ coverage for the given array configuration (ALMA-7) at the observing frequency of 100 GHz. (d) The PSF (in arcsec) for the given array configuration at 100 GHz.

possess a resolution of 0.7 arcsec/pixel, only very compact array configurations fulfill this requirement for observations² at $\lambda = 1$ mm. As we assume that prominence observations have rather extended ALMA configurations in the future (to reach higher spatial resolution), we also excluded the 1 mm case and only kept the 3 mm map for the current simulations.

To work with a slightly poorer angular resolution than the pixel size, around 1 arcsec at 100 GHz, we chose the array configuration saved at file.com//data/alma/simmos/alma.out07.cfg in the standard CASA distribution (further referred as to ALMA-7 configuration). This is a standard configuration of the full ALMA main array (fifty 12 m antennas), with a compact distribution; see Figure 7(b).

As we just explained, the selected ALMA configuration and observing frequency are limited by the requirement that the model image needs to have a resolution higher than the simulated ALMA observation. This is usually not a problem in models based on numerical simulations; see *e.g.* Wedemeyer-Böhm and Rouppe van der Voort (2009). However, in our case, the model image is based on optical observation with a moderate resolution, and we are therefore forced to simulate rather low-resolution ALMA observations. Nevertheless, more extended ALMA configurations together with a higher observing frequency can (and shall) be used to reach an unprecedented resolution of up to 0.005 arcsec. This will definitely bring new insight into the physics of prominences; however, such a high resolution is beyond the scope of our current model.

²See http://casaguides.nrao.edu/index.php?title=Antenna_List.

The estimated values of the brightness temperature reach ≈ 3000 K at 100 GHz (Figure 3(b)). This is still well within the dynamical range of ALMA Band 3 detectors (they saturate at ≈ 5000 K; see Sramek *et al.*, 2012) without using the attenuators intended specifically for solar observations. This facilitates calibration and enables the usage of water-vapor radiometer measurements for phase corrections (Sramek *et al.*, 2012). Thus, the solar prominences may play the role of experimental targets in early solar observations with ALMA. It should be noted, however, that the observation of solar prominences brings another challenge connected to the difficulties related to deconvolution or cleaning of large-scale diffuse structures in general. Moreover, specifically for prominences, the effects of side beams of the interferometer that can bias the observations on the solar limb by a much stronger signal from the disk need to be taken into account (results of the third Solar ALMA campaign: M. Shimojo and T. Bastian, private communication). On the other hand, the recently suggested approach of SIS-mixer detuning (Asayama, Whyborn, and Yagoubov, 2012) can make even brighter solar targets accessible without using solar attenuators with all their drawbacks (Sramek *et al.*, 2012).

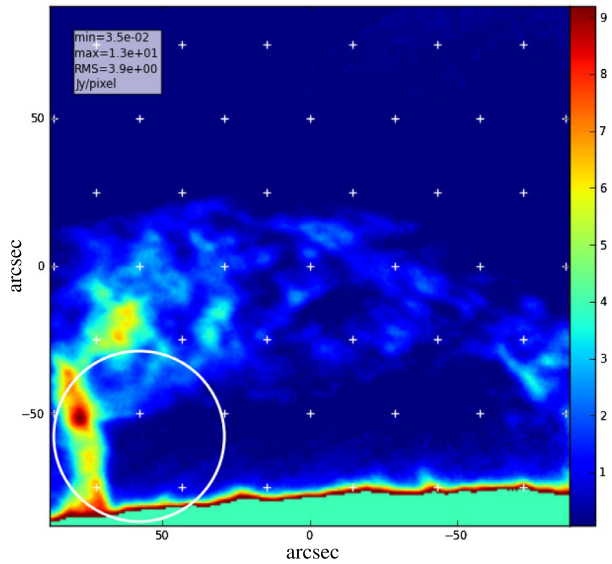
High-resolution interferometric observations of prominences are somewhat challenging because of the large scale-separation between the desired angular resolution (the smallest scale) and the quite large dimensions of the entire prominence. This may result in a large mosaic – an interferometric image composed of more individual fields of view, with many pointings. The large mosaics are not only technically expensive, but their observing time can easily reach the characteristic dynamical time (typically minutes – see below) in the studied object. Hence, there always is a trade-off between the field of view, angular, and temporal resolutions. For this reason we selected a 256×256 pixel area from the initial brightness-temperature model map at 3 mm, as indicated in Figure 1.

Figure 7 shows the key parameters for the selected ALMA configuration (ALMA-7), observing frequency (100 GHz), date (21 April 2013), and the target (the Sun). Panel (a) shows the height of the target above the local horizon at the ALMA site for the date of the simulated observation, panel (b) displays the distribution of antennas of the ALMA main array in the ALMA-7 configuration, panel (c) shows the corresponding $u - v$ coverage for a single observed spectral window (see below), and panel (d) is the point spread function (PSF) of the array at 100 GHz.

The selected area of 180 arcsec^2 leads to a medium-sized mosaic with 45 pointings (see Figure 8) that shows the pointing centers overlaid on the background of the model brightness. The estimation made using ALMA sensitivity calculator – the part of the ALMA OT package³ – gives a value of ≈ 2 min for the total observing time (including calibrations) with a sensitivity of 3 K. This sensitivity corresponds to a reasonably high dynamical range 1:1000 (the highest model brightness temperature reaches ≈ 3000 K). The observing time of 2 min is still acceptable with respect to the characteristic dynamic time of prominence fine structures that was recently revealed from *Hinode/SOT* observations (see the review by Parenti (2014) and references therein). Moreover, the sensitivity calculator shows that just 10 s are spent observing the science target (prominence; see below), and next 8 s are required for phase calibration. These two scans will be repeated in a longer scheduling block aimed at observing the prominence dynamics. The rest of the time is spent by band-pass, flux, pointing, and atmospheric calibrations that are performed only once at the very beginning of the scheduling block. The calibration times mentioned here are, however, just for

³(ALMA Observing Tool, see <http://almascience.eso.org/call-for-proposals/observing-tool>; the stand-alone Java-based web interface to the sensitivity calculator also exist at <http://almascience.eso.org/call-for-proposals/sensitivity-calculator>.)

Figure 8 Simulated ALMA pointing centers (mosaicking) overlaid on the background model radio map. Color scale is in units of Jy/pixel.



quick orientation; they can vary with the season as different calibrators are available in the vicinity of the Sun during the year.

The values above were estimated for the parameters used in our simulated observations, namely for the observing frequency of 100 GHz. Nevertheless, envisaged high-resolution ALMA observations will be more likely made at shorter wavelengths. In this case, the number of pointings and hence also the time spent on the source will increase with the square of the observing frequency. For example, observations performed at ≈ 600 GHz will require 6^2 times more pointings and thus (assuming the same relative sensitivity) also 36 times more time spent on source. As for the simulated observation at 100 GHz, the time-on-source estimated by the ALMA OT is 10.0 s; for observations at 600 GHz, the time spent on source is expected to be ≈ 6 min and the total observing time ≈ 8 min. Hence, for the detailed studies of the ultra-fine prominence structures with ALMA, a smaller subarea of a prominence will probably have to be selected.

We applied two different setups of simulated observation. The simple one (referred to as Setup 1) uses a single spectral window (SPW) centered around 100 GHz in which a continuum of the bandwidth 1875 MHz (a maximum SPW bandwidth) is observed. The second, more realistic setup (Setup 2), fully uses the lower side (LSB) and upper side (USB) ALMA basebands (checked in ALMA OT), defining four SPWs centered around the frequencies 93 GHz, 95 GHz, 105 GHz, and 107 GHz. In each of them, again, the continuum of the bandwidth 1875 MHz is observed. For weak sources, this setup is used for performance enhancement (larger total bandwidth – shorter observing time with a given desired sensitivity). However, for solar observations, the total observing time is mostly given by ‘service’ tasks (re-pointing, calibrator observations). Nevertheless, it can help to improve the $u-v$ coverage when the multi-frequency synthesis (MFS) mode is used for imaging with the clean() CASA task. This can be important for diffuse sources observed with a short time-integration – just as in the case of solar prominences. The results from the two setups are compared below (Figure 10).

Interferometric imaging of prominences – and other diffuse large-scale structures on the Sun – is a challenging task in any case. Early commissioning and science-verification ob-

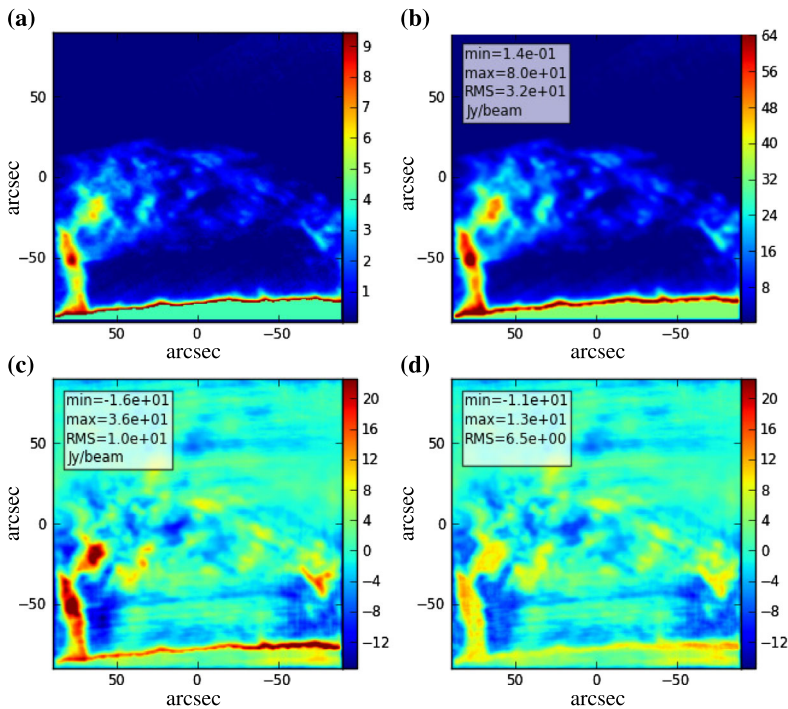


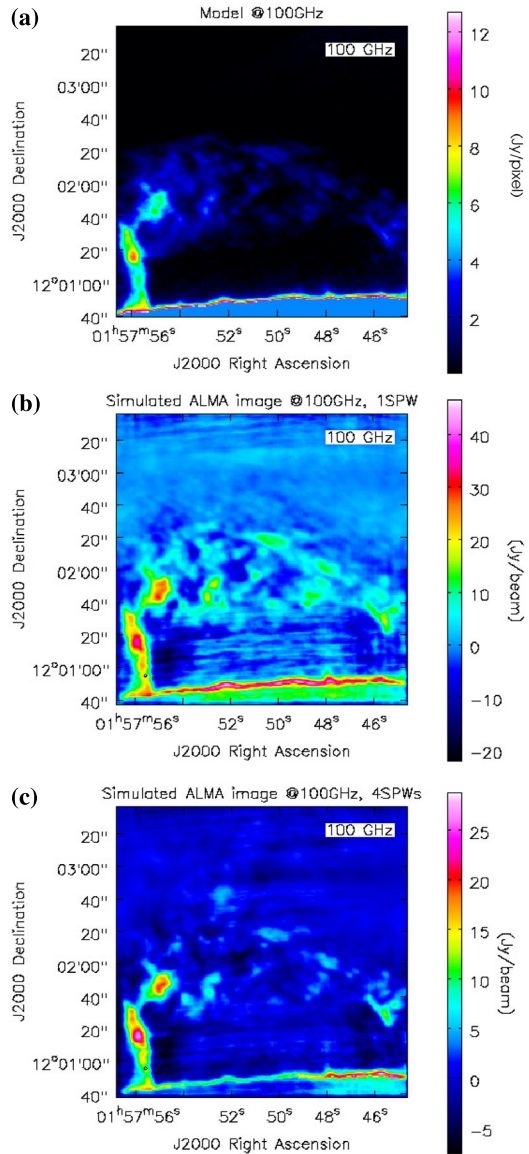
Figure 9 Output of the CASA `simanalyze()` tool. (a) Input model radio brightness map recalculated to Jy/pixel. (b) Input model radio brightness map recalculated to Jy/beam. (c) Simulated ALMA observations with four SPWs; radio brightness in Jy/beam. (d) Simulated residual map after `clean()` applied in the CASA `simanalyze()` tool.

servations (the third Solar ALMA campaign; M. Shomijo and T. Bastian, private communication) have shown the essential role of the *Atacama Compact Array* (ACA) for imaging of extended solar targets. Furthermore, alternative deconvolution algorithms like the Maximum Entropy Method (MEM; now experimental in CASA) should be developed and tested for diffuse large-scale solar structures.

The simulated observation was also analyzed by a convenient CASA task `simanalyze()` that takes care of the imaging procedure and subsequently calculates and displays a comparison with the input model to estimate the fidelity of the image reconstructed from the simulated observation. Such an analysis is presented in Figure 9. Panel (a) shows the original model contained in the input FITS file with the brightness in Jy/pixel. Panel (b) represents its recalculation into Jy/beam. Panel (c) represents the reconstructed image of the simulated observation (CASA measurement set, MS) with four SPWs centered around 100 GHz (Setup 2), and panel (d) shows the residual image after the `clean()` procedure. Imaging in `simanalyze()` was done on a best-effort basis; not only the default dirty image was gained in this way. Nevertheless, many image components clearly remain in the residual image. This is essentially related to the diffuse nature of the solar prominences. Consequently, it is practically impossible to define the usual cleaning mask. Future image-processing algorithms more suitable for this type of sources like MEM might improve ALMA's performance in image restoration.

As an alternative to `simanalyze()`, we tried the standard `clean()` task as it allows for more flexibility. Above all, for the diffuse sources with a poor $u-v$ coverage (because of the

Figure 10 Comparison between model and simulated-observation radio maps. (a) Model radio emission for $T = 8000$ K and EM derived from the observed $H\alpha$ image. (b) Simulated ALMA radio map. The simulated observation has been done at a single 1875 MHz wide spectral window (SPW) centered at 100 GHz. (c) Simulated ALMA radio map: four 1875 MHz wide SPWs centered at 93 GHz, 95 GHz, 105 GHz, and 107 GHz have been observed simultaneously. Color scale in Jy/beam.



short time spent on the target source in our case), the recommended PSF mode is ‘hogbom’ with Briggs weighting.⁴ Furthermore, the multi-scale cleaning can be conveniently set up. The results of the cleaning procedure with ‘hogbom’ PSF-mode, Briggs weighting (robustness = 0.5), and multi-scale cleaning (with scales of 0, 5, 10, and 15 pixels) for 2000 iterations are shown in Figure 10. Panel (a) shows the model brightness that entered the `simobserve()` task, and panels (b) and (c) show the reconstructed images from simulated observations with Setup 1 (a single SPW) and Setup 2 (four SPWs), respectively. The

⁴See *CASA cookbook*, <http://casa.nrao.edu/docs/userman/UserMan.html>.

simulated observation with Setup 2 clearly provides the image with a higher fidelity than that with a single continuum in one SPW because of improved $u - v$ coverage (and the MFS mode used in the imaging procedure). Figure 10(c) shows an image that is qualitatively closer to the original mode (Figure 10(a)) and that is biased by much fewer imaging artifacts than Figure 10(b). Extrapolating this finding further, it might be useful to split the SPWs into (moderate width) frequency channels. Since the targets on the Sun are usually bright enough, this fragmentation of the total bandwidth should not lead to significant decrease in the observing performance (increase in the total observing time) until a really high frequency resolution is reached. The bonus is, on the other hand, clear – more channels can improve the $u - v$ coverage even further. We will investigate this possibility in our future studies.

However, in spite of qualitative improvement (fewer artifacts in the image) for channeled continuum observations with subsequent MFS cleaning, a quantitative comparison with the model image shows that the emission was decreased by a factor of ≈ 2 in the simulated observation. This is related to the difficulties described above in imaging of diffuse objects with standard *clark* or *highbom* cleaning methods. The practical impossibility of defining a cleaning mask for these algorithms causes many flux components to remain in the residual image. Consequently, the number of restored image components is insufficient. Future methods like MEM will hopefully limit this issue.

6. Discussion and Conclusions

We have performed simulations of the brightness temperature of a quiescent prominence that was originally observed in the $H\alpha$ line by the Wrocław MSDP instrument. In particular, we focused on the fine structures, using the $H\alpha$ maps at a moderate spatial resolution of about 1–2 arcsec. The brightness temperatures were computed for SMM wavelengths in the range of the ALMA radio-interferometer. Subsequently, we used these predicted radio maps as input for the ALMA image simulations, using the CASA software. This shows how the prominence visible in $H\alpha$ will look like in the ALMA radio domain, and specifically, we showed the maps for the wavelength of 3 mm. However, our simulations of the ALMA visibility are more illustrative than comprehensive. The problem of selecting the optimal wavelength windows that would cover the range of SMM spectra that are suitable for realistic temperature diagnostics, as well as the problem of ALMA solar filters, is much more complex, and the actual observational setup has to be optimized. This article also contains a detailed discussion of the SMM continuum formation under typical prominence conditions. ALMA is planned to detect the central coolest parts of the prominence fine structures. Their expected form is a magnetic dip filled by cool ($T < 10^4$ K) plasma (Gunár *et al.*, 2013; Hillier and van Ballegoijen, 2013). Quite recently, Gunár and Mackay (2015) have constructed a 3D model of the prominence fine structure where the magnetic dipoles contain cool plasma in their innermost parts and are surrounded by a PCTR. The spatial resolution is only a numerical one (reaching a few km), and thus this kind of prominence structure can be used in the future for high-resolution simulations of radio images. The relevant SMM observations represent an ultimate goal of the ALMA instrument.

We have mentioned possible ways of determining the prominence kinetic temperature, provided that the LOS temperature structure is more or less uniform within the fine-structure threads. By fitting the broadband ALMA spectra, both the kinetic temperature and optical thickness can be derived. Simultaneous $H\alpha$ observations with high spatial resolution would

also help in determining the optical thickness independently of the SMM observations. However, in reality the temperatures and density structure of quiescent prominences will be non-uniform (variations along the LOS and PCTR), and this should be accounted for by forward modeling based *e.g.* on the fine-structure dip models mentioned above. Then the synthetic spectrum will be directly compared with that obtained by ALMA to check the reliability of these models.

Brightness temperature maps of a quiescent prominence were simulated using the existing H α data. However, even when obtained with a large coronagraph, these observations provide a moderate spatial resolution of between 1–2 arcsec. This is at least a factor of five lower in resolution than is currently achieved by large telescopes on ground or in space. The latest *Hinode*/SOT H α or Ca II H line images or movies show a wide variety of highly dynamical fine structures (Berger *et al.*, 2008; Heinzel *et al.*, 2008). Therefore, it would be useful as a next step to obtain *calibrated* H α data from these instruments (*e.g.* *Hinode*/SOT) and apply to them the same simulation procedure as in the present article. We note that at higher spatial resolution, the surface filling factor mentioned in Section 2 will go to unity and thus, according to Equation (10), T_b will increase. This means that with our moderate resolution, we obtained maps of T_b representing a lower-limit estimate of the brightness temperatures detectable with ALMA that will eventually resolve the prominence fine structures that are not visible in our simulations. Simultaneous test observations with ALMA and large optical telescopes would be worth trying. Based on the present results, we will plan the first ALMA science and technical verification tests.

Acknowledgements We dedicate this article to the memory of our colleague and friend Stanislav (Stan) Stefl, who spent his last time at the ALMA facility in Chile. PH acknowledges support from grant 209/12/0906 of the Grant Agency of the Czech Republic. MB and MK acknowledge support from grant P209/12/0103 of the Grant Agency of the Czech Republic. This work was supported by the institutional project RVO 67985815 of the Astronomical Institute of the Academy of Sciences of the Czech Republic. This research was partially performed under the support of the European Commission through the CIG grant PCIG-GA-2011-304265 (SERAF) and grant 13-24782S of the Grant Agency of the Czech Republic. MB thanks Anita M. Richards for helpful discussions of the ALMA simulations. We also thank Ulrich Anzer for helpful discussions and the anonymous referee for very useful comments and suggestions.

References

- Asayama, S., Whyborn, N., Yagoubov, P.: 2012, In: Holland, W.S. (ed.) *Millimeter, Submillimeter, and Far-Infrared Detectors and Instrumentation for Astronomy VI*, *Proc. SPIE* **8452**, 84522Z.
- Bastian, T.S., Ewell, M.W., Zirin, H.: 1993, *Astrophys. J.* **418**, 510.
- Benz, A.O.: 1993, *Plasma Astrophysics*, Kluwer Academic, Dordrecht, 263.
- Berger, T.E., Shine, R.A., Slater, G.L., Tarbell, T.D., Title, A.M., Okamoto, T.J., *et al.*: 2008, *Astrophys. J.* **676**, 89.
- David, K.: 1961, *Z. Astrophys.* **53**, 37.
- Dulk, G.A.: 1985, *Annu. Rev. Astron. Astrophys.* **23**, 169.
- Engvold, O., Hirayama, T., Leroy, J.-L., Priest, E.R., Tandberg-Hanssen, E.: 1990, In: Ruzdjak, V., Tandberg-Hanssen, E. (eds.) *Dynamics of Quiescent Prominences, Lecture Notes in Physics* **363**, Springer, Berlin 294.
- Gopalswamy, N., Hanaoka, Y., Lemen, J.R.: 1998, In: Webb, D.F., Schmieder, B., Rust, D.M. (eds.) *New Perspectives on Solar Prominences, ASP Conf. Ser.* **150**, 358.
- Gouttebroze, P.: 2007, *Astron. Astrophys.* **465**, 1041.
- Gouttebroze, P., Heinzel, P., Vial, J.-C.: 1993, *Astron. Astrophys. Suppl.* **99**, 513.
- Gunár, S.: 2014, In: Schmieder, B., Malherbe, J.-M., Wu, S.T. (eds.) *Nature of Prominences and Their Role in Space Weather, IAU Symp.* **300**, 59.
- Gunár, S., Mackay, D.H., Anzer, U., Heinzel, P.: 2013, *Astron. Astrophys.* **551**, 3.
- Gunár, S., Mackay, D.H.: 2015, *Astrophys. J.*, submitted.
- Gunár, S., Heinzel, P., Anzer, U., Schmieder, B.: 2008, *Astron. Astrophys.* **490**, 307.

- Gunár, S., Mein, P., Schmieder, B., Heinzel, P., Mein, N.: 2012, *Astron. Astrophys.* **543**, 93.
- Harrison, R.A., Carter, M.K., Clark, T.A., Lindsey, C., Jefferies, J.T., Sime, D.G., *et al.*: 1993, *Astron. Astrophys.* **274**, L9.
- Heasley, J.N., Mihalas, D.: 1976, *Astrophys. J.* **205**, 273.
- Heinzel, P.: 2014, In: Vial, J.C., Engvold, O. (eds.) *Solar Prominences*, Springer, Berlin 103.
- Heinzel, P., Anzer, U.: 2001, *Astron. Astrophys.* **375**, 1082.
- Heinzel, P., Anzer, U.: 2014, *Astron. Astrophys.* **539**, 49.
- Heinzel, P., Avrett, E.H.: 2012, *Solar Phys.* **277**, 31.
- Heinzel, P., Gouttebroze, P., Vial, J.-C.: 1994, *Astron. Astrophys.* **292**, 656.
- Heinzel, P., Schmieder, B., Fárnik, F., Schwartz, P., Labrosse, N., Kotrč, P., *et al.*: 2008, *Astrophys. J.* **686**, 1383.
- Hillier, A., van Ballegooijen, A.: 2013, *Astrophys. J.* **766**, 126.
- Hirayama, T.: 1990, In: Ruzdjak, V., Tandberg-Hanssen, E. (eds.) *Dynamics of Quiescent Prominences, Lecture Notes in Physics* **363**, Springer, Berlin 187.
- Irimajiri, Y., Takano, T., Nakajima, H., Shibasaki, K., Hanaoka, Y., Ichimoto, K.: 1995, *Solar Phys.* **156**, 363.
- Jejčič, S., Heinzel, P.: 2009, *Solar Phys.* **254**, 89.
- Karlický, M., Bárta, M., Dabrowski, B.P., Heinzel, P.: 2012, *Solar Phys.* **268**, 165.
- Karzas, W.J., Latter, R.: 1961, *Astrophys. J. Suppl.* **6**, 167.
- Kurucz, R.L.: 1970, SAO Special Rep. **309**, Smithsonian Astrophysical Observatory.
- Labrosse, N., Heinzel, P., Vial, J.-C., Kucera, T., Parenti, S., Gunár, S., Schmieder, B., Kilper, G.: 2010, *Space Sci. Rev.* **151**, 243.
- Loukitcheva, M., Solanki, S.K., Carlsson, M., Stein, R.F.: 2004, *Astron. Astrophys.* **419**, 747.
- Mein, P.: 1991, *Astron. Astrophys.* **248**, 669.
- Mihalas, D.: 1978, *Stellar Atmospheres*, 2nd edn. Freeman, San Francisco, 225.
- Parenti, S.: 2014, *Living Rev. Solar Phys.* **11**(1). <http://solarphysics.livingreviews.org/Articles/lrsp-2014-1/>.
- Rompolt, B., Mein, P., Mein, N., Rudawy, P., Berlicki, A.: 1994, In: von Alvensleben, A. (ed.) *JOSO Annual Report 1993*, Joint Organization for Solar Observations, 87.
- Rybicki, G.B., Lightman, A.P.: 1979, *Radiative Processes in Astrophysics*, Wiley, New York, 162.
- Schmieder, B., Chandra, R., Berlicki, A., Mein, P.: 2010, *Astron. Astrophys.* **514**, 68.
- Sramek, R., Morita, K., Sugimoto, M., Napier, P., Miccolis, M., Yagoubov, P., *et al.*: 2012, In: Stepp, L.M., Gilmozzi, R., Hall, H.J. (eds.) *Ground-Based and Airborne Telescopes IV, Proc. SPIE* **8444**, 84442K.
- Tsuneta, S., Suematsu, Y., Ichimoto, K., Shimizu, T., Otsubo, M., Nagata, S., *et al.*: 2008, *Solar Phys.* **249**, 167.
- Wedemeyer-Böhm, S., Rouppe van der Voort, L.: 2009, *Astron. Astrophys.* **503**, 225.